Monthly Notices of the ROYAL ASTRONOMICAL SOCIETY
MNRAS **511,** 4710–4723 (2022) https://doi.org/10.1093/mnras/stab3619

Planet Hunters TESS IV: a massive, compact hierarchical triple star system TIC 470710327

N. L. Eisner [1,2★] C. Johnston [2,3] S. Toonen,[4] A. J. Frost [2] S. Janssens [2] C. J. Lintott [1] S. Aigrain,[1] H. Sana [2] M. Abdul-Masih [5] K. Z. Arellano-Córdova,[6,7] P. G. Beck,[7,8] E. Bordier,[2,5] E. Cannon [2] A. Escorza,[5] M. Fabry,[2] L. Hermansson,[9] S. B. Howell,[10] G. Miller,[1] S. Sheyte,[11] S. Alhassan,[12] E. M. L. Baeten,[12] F. Barnet,[12,13] S. J. Bean,[12] M. Bernau,[12] D. M. Bundy,[12] M. Z. Di Fraia [12] F. M. Emralino,[12] B. L. Goodwin,[12] P. Hermes,[12] T. Hoffman,[12] M. Huten,[12] R. Janíček,[12] S. Lee,[12] M. T. Mazzucato,[12] D. J. Rogers,[12] M. P. Rout [12,14] J. Sejpka,[12] C. Tanner,[12] I. A. Terentev[12] and D. Urvoy[12]

[1]*Sub-department of Astrophysics, University of Oxford, Keble Rd, Oxford OX1 2JD, UK*
[2]*Institute of Astronomy, KU Leuven, Celestijnenlaan 200D, B-3001 Leuven, Belgium*
[3]*Department of Astrophysics, IMAPP, Radboud University Nijmegen, PO Box 9010, NL-6500 GL Nijmegen, The Netherlands*
[4]*Anton Pannekoek Institute for Astronomy, University of Amsterdam, NL-1090 GE Amsterdam, The Netherlands*
[5]*European Southern Observatory, Alonso de Córdova 3107, Vitacura, Casilla 19001, Santiago de Chile, Chile*
[6]*Department of Astronomy, The University of Texas at Austin, 2515 Speedway, Stop C1400, Austin, TX 78712, USA*
[7]*Instituto de Astrofísica de Canarias, E-38200 La Laguna, Tenerife, Spain*
[8]*Institute of Physics, University of Graz, NAWI Graz, Universitätsplatz 5/II, 8010 Graz, Austria*
[9]*Sandvretens Observatory, Linnégatan 5A, SE-75332 Uppsala, Sweden*
[10]*NASA Ames Research Center, Moffett Field, CA 94035, USA*
[11]*Institute of Astronomy and Astrophysics (IAA), Université libre de Bruxelles (ULB), CP 226, Boulevard du Triomphe, B-1050 Bruxelles, Belgium*
[12]*Citizen Scientist, Zooniverse c/o University of Oxford, Keble Road, Oxford OX1 3RH, UK*
[13]*Department of Mathematics, Frostburg State University, Frostburg, MD 21532, USA*
[14]*The Rockefeller University, 1230 York Avenue, New York, NY 10065 USA*

Accepted 2021 November 27. Received 2021 November 23; in original form 2021 July 15

ABSTRACT

We report the discovery and analysis of a massive, compact, hierarchical triple system (TIC 470710327) initially identified by citizen scientists in data obtained by NASA's *Transiting Exoplanet Survey Satellite* (*TESS*). Spectroscopic follow-up observations obtained with the HERMES spectrograph, combined with eclipse-timing variations (ETVs), confirm that the system is comprised of three OB stars, with a compact 1.10 d eclipsing binary and a non-eclipsing tertiary on a 52.04 d orbit. Dynamical modelling of the system (from radial velocity and ETVs) reveal a rare configuration wherein the tertiary star (O9.5-B0.5V; 14–17 $M_\odot$) is more massive than the combined mass of the inner binary (10.9–13.2 $M_\odot$). Given the high mass of the tertiary, we predict that this system will undergo multiple phases of mass transfer in the future, and likely end up as a double neutron star gravitational wave progenitor or an exotic Thorne–Żytkow object. Further observational characterization of this system promises constraints on both formation scenarios of massive stars as well as their exotic evolutionary end-products.

Key words: binaries(including multiple): close – stars: individual: TIC 470710327 – stars: massive.

1 INTRODUCTION

Despite their intrinsic rarity implied by the initial mass function (IMF; see, e.g. Salpeter 1955; Bastian, Covey & Meyer 2010; Dib, Schmeja & Hony 2017), massive stars ($M \geq 8$ $M_\odot$) provide radiative, dynamical and chemical feedback to their environment, driving evolution on a wide range of scales. The physical processes responsible for the formation, evolution, and death of massive stars, however, are not well understood (e.g. Zinnecker & Yorke 2007; Tan et al. 2014). The study of these processes is further complicated by the fact that such stars often have nearby stellar companions (Sana et al. 2012), which can affect their properties and evolution at all stages of their lives. Large-scale spectroscopic, interferometric, and high contrast imaging surveys of OB stars have demonstrated that most, if not all, massive stars are formed in a binary or higher order multiple system (Kiminki & Kobulnicky 2012; Sana et al. 2013, 2014; Aldoretta et al. 2015; Moe & Di Stefano 2017; Maíz Apellániz et al. 2019; Rainot et al. 2020; Bodensteiner et al. 2021)

The identification and characterization of massive stars in multiple systems is crucial to discriminate between different formation and evolution scenarios, to place constraints on theoretical models and to understand the interactions and effects of multiple stars. Sana et al. (2012) and de Mink et al. (2014) have already shown that the complex interactions between tides, angular momentum exchange, and stellar

★ E-mail: nora.eisner@new.ox.ac.uk

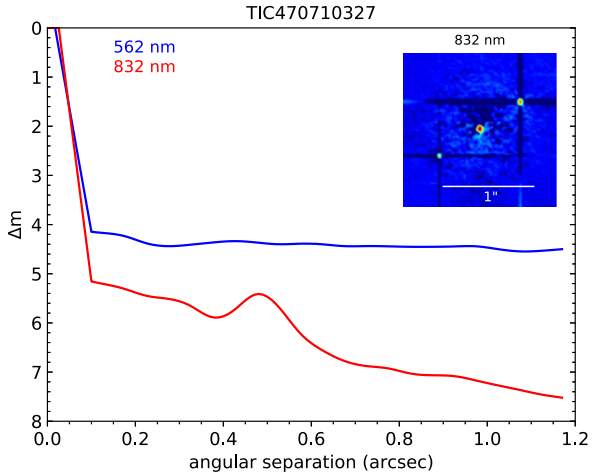

Figure 1. Contrast curves showing the 5σ detection sensitivity and the speckle reconstructed image for filters centred on 562 nm (blue) and 832 nm (red).

evolution in binary and higher order multiples fundamentally affect the evolution and thus the end product of nearly 70 per cent of all early-type massive stars. In compact binary orbits, for example, processes including mass transfer, exchange of angular momentum and stellar mergers can open up new evolutionary pathways and end-products such as X-ray binaries, γ-ray bursts, stellar mergers, and gravitational wave events (Sana et al. 2012; de Mink et al. 2013). The addition of a nearby third body further complicates the evolution. Interactions between three stars can induce different evolutionary pathways through von Zeipel–Kozai–Lidov cycles (ZKL; von Zeipel 1910; Kozai 1962; Lidov 1962; Naoz 2016; Ito & Ohtsuka 2019), or result in tertiary-driven mass transfer that can lead to mergers, exotic common-envelope systems, close double or triple degenerate systems, or contribute to the population of walk-away and run-away systems in our galaxy (Antonini, Toonen & Hamers 2017; Renzo et al. 2019; Stephan et al. 2019; Leigh et al. 2020a; Glanz & Perets 2021; Hamers et al. 2021b).

Due to the high intrinsic brightness of massive stars, detecting and characterizing non-eclipsing lower mass close companions using spectroscopy alone is challenging. Detailed characterization of close companions, therefore, often relies on the detection of eclipses or other dynamical effects caused by the presence of a close companion, such as using radial velocity (RV) observations or observations of light travel time effects via eclipse-timing variations (ETVs). Observations of the latter were made possibly with the advent of space-based photometric surveys with long time-base, high-precision, and high-cadence observations such as CoRoT, *Kepler*, *K*2, and *TESS*. These space-based missions have enabled the detection of dozens of new triple and higher order multiple systems through ETVs or multiply eclipsing events (Conroy et al. 2014; Marsh, Armstrong & Carter 2014; Borkovits et al. 2015; Hajdu et al. 2017; Rappaport et al. 2017; Li et al. 2018; Sriram et al. 2018; Borkovits et al. 2021). Detailed modelling of such systems can lead to the determination of the absolute masses of the stellar components in some cases, or minimally the derivation of mass ratios, even in the absence of eclipses (Borkovits et al. 2016).

Further considerations beyond light travel time effects need to be made for triple systems where the inner stellar binary is orbited by a third body with a longer period, known as a hierarchical triple system. Such a configuration can result in measurable dynamical perturbations to the orbit of the inner binary. If the orbital periods and the separations involved are short enough, these effects can be studied with a combination of ETVs (caused by light travel time effects and direct third-body perturbations) and/or RV observations. Measurements of both ETVs and RVs allows for the determination of precise stellar mass ratios and orbital parameters, including the mutual inclination between the inner and the outer orbit of the triple, which is thought to be indicative of the formation history.

In this paper, we present a new compact, hierarchical triple system identified in *TESS* data consisting of one O- and two B-type stars. The system, which shows large ETV and RV variations, contains an inner ∼1.1 d eclipsing binary and a massive O9.5-B0.5V tertiary orbiting a common centre of mass in a ∼52 d orbit. The discovery of the system and the data are discussed in Sections 2–4. Section 5 outlines the analysis of the photometric and spectroscopic data and Section 6 discusses the system configuration, stability, formation and possible future evolution scenarios. Finally, the conclusions are presented in Section 7.

2 THE TARGET AND ITS SURROUNDINGS

TIC 470710327 (BD + 61 2536, TYC 4285-3758-1, $V = 9.6$ mag, parallax $= 1.06 \pm 0.24$ mas, distance $= 950 \pm 220$ pc) was initially identified as an early B-type star by Brodskaya (1953) and as a short period eclipsing binary with a period of 1.1047 d using photometric data obtained with the 0.25-m Takahashi Epsilon telescope in Mayhill, New Mexico, USA (Laur et al. 2017). The target is not a known member of a cluster or OB association (Laur et al. 2017). Two epochs of speckle interferometric measurements revealed a close companion at ∼0.5 arcsec, with the position angle and distance of the companion advancing from $\theta = 306.^{\circ}2$ and $\rho =$ 0.533 arcsec in 1987.7568 (Hartkopf et al. 2000) to $\theta = 303.^{\circ}7$ and $\rho = 0.502$ arcsec in 2003.9596 (Hartkopf, Mason & Rafferty 2008).

In order to calculate the magnitude differences between TIC 470710327 and the ∼0.5 arcsec companion, hereafter TIC 470710327′, we performed speckle imaging using the Zorro instrument on the 8.1-m Gemini South telescope on Cerro Pachón, Chile (Matson, Howell & Ciardi (Howell et al. 2011; Matson, Howell & Ciardi 2019). Observations were carried out on 2020 August 15 using the two-colour diffraction-limited optical imager with 60 msec exposures in sets of 1000 frames. The 5σ detection sensitivity and the speckle reconstructed image are shown in Fig. 1. The data confirmed that the companion star is located at an angular separation of 0.529 arcsec with a position angle of $304.^{\circ}5$, which is in agreement with previous observations (Hartkopf et al. 2000, 2008). The data showed that the companion has a magnitude difference of $\Delta m =$ 1.17 mag at 562 nm and of Δm = 1.13 mag at 832 nm.

To characterize the target's surroundings and to quantify the light contribution of nearby stars, we queried the early Gaia Data Release 3 catalog (eDR3; Gaia Collaboration et al. 2021). This search revealed a bright ($V = 11.6$, $\Delta T_{\rm mag} = 2.4$) nearby star at a separation of ∼22 arcsec (LS I + 61 72), as well as a further six stars with a $\Delta T_{\rm mag} < 5$ within 100 arcsec of the target (listed in Table 1). The light contribution of these stars to our photometric observations will be discussed in Section 3.

Overall, the triple system TIC 470710327 presented in this paper consists of a $P_1 \sim 1.1$ d eclipsing binary with a $P_2 \sim 52$ d non transiting tertiary. Hereafter, the two stars in the inner, short period binary will be referred to as stars A and B, while the tertiary on the wide, outer orbit will be referred to as star C. The 0.5 arcsec companion star will be referred to as TIC 470710327′. Using the Gaia eDR3 list of sources in a 2 arcmin radius to determine the

Table 1. Nearby GAIA eDR3 sources within 100 arcsec and $\Delta T_{\rm mag} < 5$ of the target.

2MASS Identifier	Distance (arcsec)	$\Delta\ T_{\rm mag}$	$\Delta V_{\rm mag}$
23491896 + 6157459	0.000	0.00	0.00
23491667 + 6158004	21.845	2.40	2.35
23492132 + 6157124	37.395	4.76	5.75
23492010 + 6156568	49.643	4.82	5.07
23491426 + 6157050	52.642	4.38	5.64
23490933 + 6158367	84.892	4.65	5.36
23493217 + 6157231	95.863	3.35	3.69
23492162 + 6159230	98.898	4.45	5.11

local field density, and the magnitude contrasts given by the speckle observations, we show that the spurious association probability between TIC 470710327′ and TIC 470710327 is $\sim 1 \times 10^{-5}$. This means that statistically there is an association between the target and the nearby companion. Assuming that the *Gaia* distance to this target (∼950 pc; Gaia Collaboration et al. 2018) is accurate, an angular separation between TIC 470710327′ and TIC 470710327 of 0.5 arcsec corresponds to a physical separation of approximately 500 au with an orbital period on the order of 1500-2000 yr, depending on the mass of the companion. Following this, we will for the remainder of this paper assume that their physical separation is too large for TIC 470710327′ to have any dynamical effect on the triple system on the timescales of our observations. Furthermore, we note that both the astrometric excess noise (significant at 4000 σ) and the RUWE parameter (11.9) for TIC 470710327 are large. This is to be expected for unresolved multiple systems, but can contribute to an unreliable astrometric determination (Ziegler et al. 2018; Lindegren et al. 2021). Conversely, the 22 arcsec companion has relatively small values for the RUWE parameter and astrometric excess noise, indicating that it is likely a single object.

3 PHOTOMETRIC DATA AND ETVS

3.1 *TESS*

TIC 470710327 was identified as a potential multiple system by citizen scientists taking part in the Planet Hunters TESS (PHT) citizen science project (Eisner et al. 2021). PHT, which is hosted by the Zooniverse platform (Lintott et al. 2008, 2011), has engaged nearly 30 000 registered volunteers in the search for planetary transit signals in 2-min cadence light curves obtained by the Transiting Exoplanet Survey Satellite (*TESS*, Ricker et al. 2015). In brief, each light curve is seen by 15 volunteers who identify times of transit-like events. Once a volunteer has classified a target, they are able to discuss the target on a discussion forum, and flag interesting systems to the PHT science team using searchable hashtags. TIC 470710327 was flagged as an interesting system on the discussion forum on 2019 December 6,[1] due to the light curve containing multiple periodic signals: $P_1 \sim 1.10$ d, $P_3 \sim 9.97$ d, and $P_4 \sim 4.01$ d, as shown in the bottom panel of Fig. 2. We note that for the remainder of this paper we assume that the stars associated with the P_3 and P_4 signals are not close enough to the triple to induce observable ETVs and that these signals do not originate from star C, as discussed further in Section 6.1.

TIC 470710327 was monitored by *TESS* in the 2-min cadence data during Sectors 17, 18, and 24 of the nominal mission. The full *TESS* data set, displayed in the top panel of Fig. 2, spans ∼230 d, with the first subset covering nearly 60 d continuously, followed by a large gap of 140 d, before the second ∼30 d subset of observations. Visual inspection of the full *TESS* light curve reveals a clear ∼1.10 d eclipsing binary system (Fig. 2). The presence of full eclipses, combined with clear points of ingress and egress implies that the inner binary has a high inclination (i_1), close to 90°.

The pixel aperture used to extract the light curve, as determined by the *TESS* pipeline at the Science Processing Operations Center (SPOC, Jenkins et al. 2016), is displayed as the red outline in Fig. 3. The orange circles indicate the position of nearby stars that have a *TESS* magnitude difference $\Delta T_{\rm mag} < 5$ from the target star, as queried from Gaia eDR3 (Gaia Collaboration et al. 2021). Considering all sources with a $\Delta T_{\rm mag} < 5$ within 100 arcsec of the target (listed in Table 1), we expect TIC 470710327 (including the 0.5 arcsec companion, TIC 470710327′) to contribute 88–89.5 per cent of the total light in the *TESS* light curve.

Similarly, using the magnitude contrast derived from the speckle imaging, we estimate that TIC 470710327′ contributes ∼26 per cent of the observed light at 832 nm. Thus, given the ∼10.5–12 per cent light contribution of the neighbour at 22 arcsec, we estimate that TIC 470710327 and TIC 470710327′ contribute ∼65 per cent and ∼23 per cent of the total light observed by *TESS*, respectively. As we show in Section 6.1, the signals $P_3 \sim 9.97$ d and $P_4 \sim 4.01$ d cannot be hosted by the tertiary object in TIC 470710327, but likely originate from this composite contaminating light. For the remainder of the paper, we will thus not consider their influence/contribution. Finally, we attempted to use both smaller apertures as well as centroid motions to determine the direction in which the photocentre moved during the $P_3 \sim 9.97$ d and $P_4 \sim 4.01$ d eclipses. We found no discernible motion in the centroid positions and negligible change in eclipse depths when different apertures were used. This either suggests that all signals originate from a single *TESS* pixel or that these signals have too small of a light contribution to result in a detectable centroid motion.

3.2 Additional photometric observations

In addition to the *TESS* data, there are 531 archival photometric observations obtained with the 0.25-m Takahashi Epsilon telescope in Mayhill, New Mexico, USA between 2011 and 2013 (Laur et al. 2017); 108 photometric observations taken over 600 d by the SuperWASP-N camera located on La Palma, Canary Islands (Pollacco et al. 2006); as well as 1784 photometric observations obtained since 2012 by the ASAS-SN network of telescopes (Shappee et al. 2014; Kochanek et al. 2017). We also obtained 456 photometric observations in the Johnson Cousins Bu band between 2020 March 21 and 30, using a 0.41-m RC telescope with an Optical Guidance Systems and an SBIG STL-6303E camera, located at the Sandvreten Observatory, Sweden. Finally, we obtained 1415 photometric observations using the Las Cumbres Observatory (LCO) global network of fully robotic 0.4-m/SBIG and 1.0-m/Sinistro facilities. The LCO data were reduced and calibrated using the standard LCO Banzai pipeline. For both the LCO and the Sandvreten Observatory data, we performed aperture photometry for TIC 470710327 and five comparison stars using the open source SEP package (Bertin & Arnouts 1996; Barbary 2016)

These archival and new photometric measurements significantly increased the baseline of the observations, allowing us to refine the period of the inner binary to $P_1 = 1.104\,686 \pm 0.000\,004$ d. The facilities used to obtain these measurements have significantly smaller pixel scales than *TESS*, such that the extracted light curves do

[1] https://www.zooniverse.org/projects/nora-dot-eisner/planet-hunters-tess/talk/2112/1195850?comment=2011869&page = 1

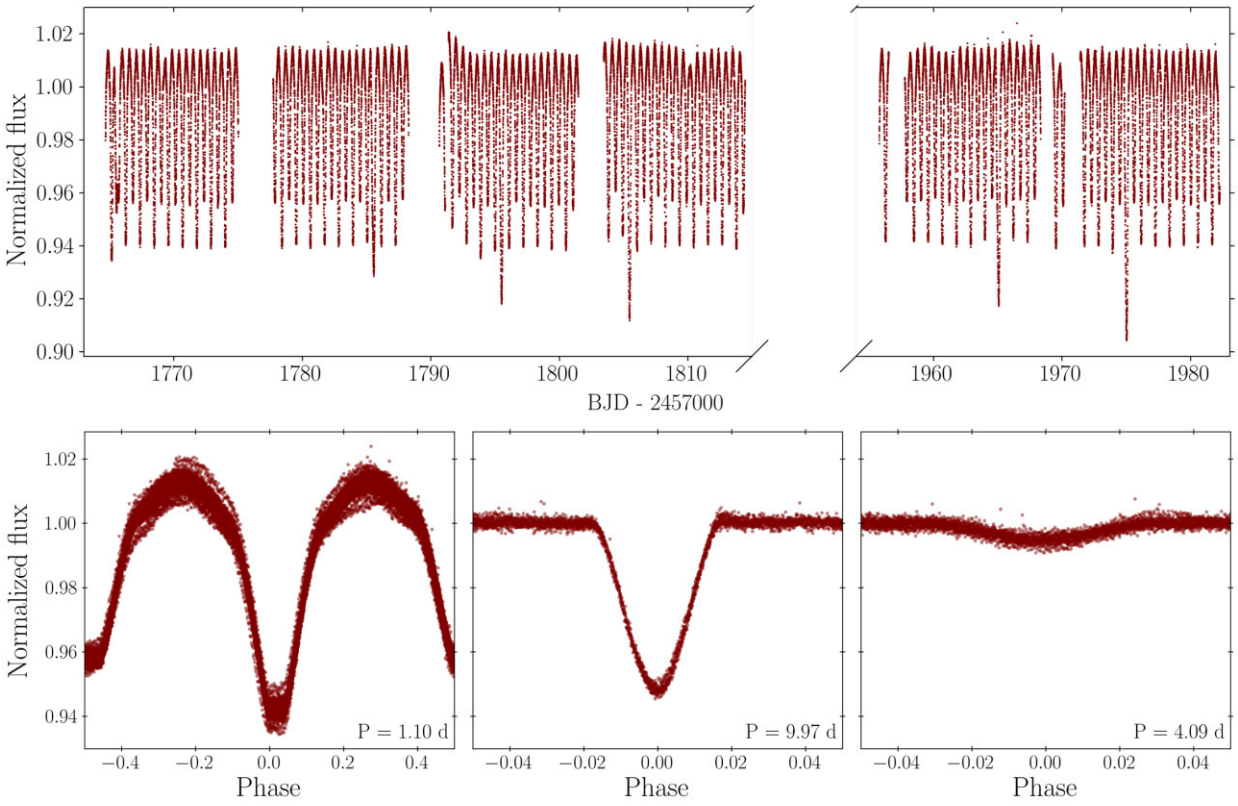

Figure 2. Top panel: full *TESS* light curve of TIC 470710327 obtained during sectors 17,18, and 24. The dashed lines on the x-axis show a split in the axis. Bottom panel: light curve phase folded on $P_1 = 1.1$ d, $P_3 = 9.97$ d, and $P_4 = 4.09$ d signals. Each panel represents one signal, where the other two signals had been masked out. Combined these three signals make up the light curve seen in the top panel. P_3 and P_4 are assumed to not be dynamically associated with the triple system presented in this paper, as discussed in Section 5.

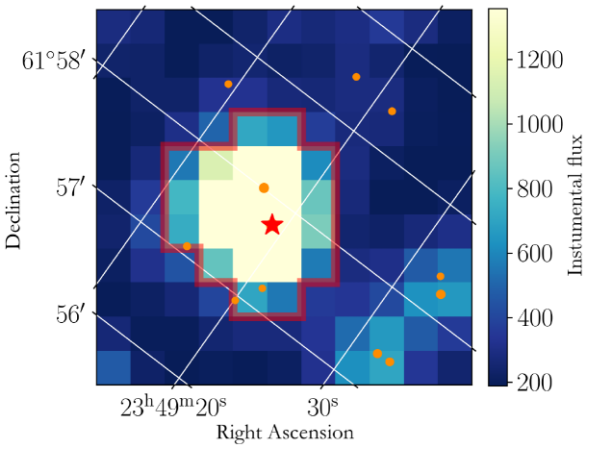

Figure 3. Average flux per pixel around TIC 470710327 obtained by *TESS* during Sector 17. The orange dots show all neighbouring stars with $V_{\rm mag} < 5\Delta T_{\rm mag}$ from the target star, as queried from Gaia eDR3 (Gaia Collaboration et al. 2021). The red outline shows the *TESS* aperture that was used to extract the flux in Sector 17.

not include TIC 470710327′. This allowed us to confirm the stability of the dominant periodic signal, $P_1 = 1.10$ d, and verify that this binary signal does not originate from TIC 470710327′. Due to the sparse sampling of these five data sets, we are unable to use these observations to investigate the stability or the origin of either the P_3 nor the P_4 signals.

3.3 Eclipse-timing variations

ETVs, which are deviations from a strictly linear ephemeris of the eclipsing binary, can be used to detect or study additional gravitating bodies in a system. While the midpoint of eclipses of an isolated eclipsing binary are expected to occur at regular time intervals, dynamical perturbations from additional bodies, such as in a hierarchical triple system, can result in periodic deviations from the expected times of the eclipses. We searched for deviations from the predicted linear ephemeris of P_1, given by

$$T_{\rm min,P/S} = t_{0,P/S} + 1.104686 \times (E),$$

where E is the cycle number since the reference orbit, $t_{0,P} = 2458766.2700$ is the reference epoch for primary eclipses, and $t_{0,S} = 2458766.82234$ is the reference epoch for secondary eclipses.

Using the *TESS* data alone, we determined the deviations from this ephemeris following the methodology outlined by Li et al. (2018). In brief, we determined the eclipse regions of the primary and secondary eclipses by extracting the minima of the second derivative around the time of the eclipses in the phase folded light curve. These translate to the phases of ingress and egress. Prior to this, we masked the $P_3 = 9.9733$ d signal from the light curve. The lower amplitude signal from P_4 was not removed due to the risk of introducing spurious signals.

Next, we generated a model of the primary eclipse by fitting a trapezoid (the shape found to best represent the eclipses) to the smoothed, phase folded and subsequently binned light curve. This model was then fit to each individual primary transit where the only two free model parameters were the time of eclipse and

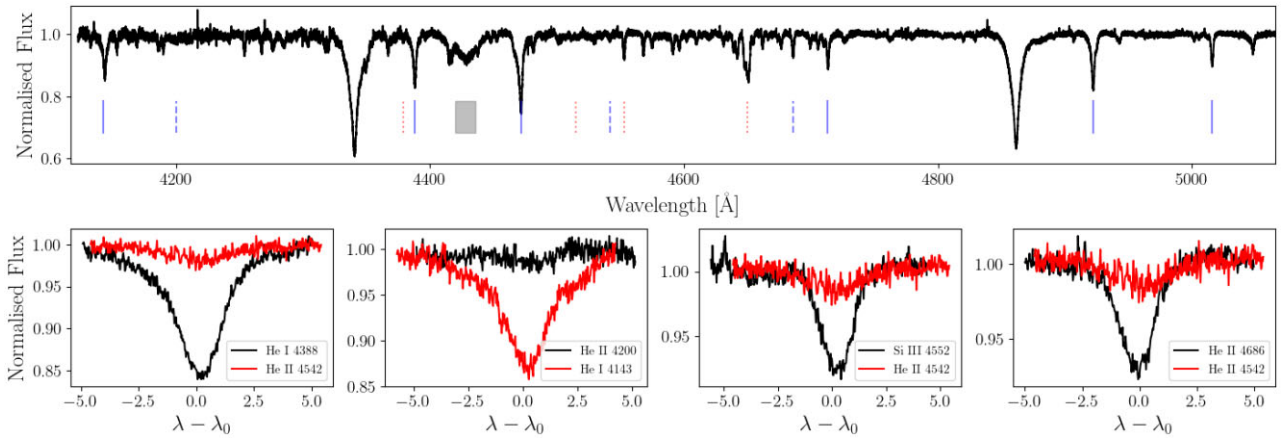

Figure 4. Top panel: Shifted and median combined HERMES spectra of TIC 470710327 A (S/N > 80). Solid vertical blue lines denote He I lines, dashed vertical blue lines denote He II lines, dotted red lines denote metal lines, and the shaded grey region denotes a diffuse interstellar band. Bottom panel: each panel displays a set of two lines used for diagnostic determination of spectral classification by Sota et al. (2011).

the slope of an underlying linear trend. The latter was to allow for systematic effects that change the slope of the eclipse. The same methodology was independently carried out for the secondary eclipses. The individual fits to all eclipses, including both the primary and the secondary eclipses of the $P_1 = 1.1047$ d signal, were optimized using a Markov chain Monte Carlo (MCMC) approach, using the open source software EXOPLANET (Foreman-Mackey et al. 2021). The observed minus calculated times of eclipse (O – C), which show variations on the range of $\sim\pm$ 6 min, are listed in Tables A2 and A3 for the primary and secondary eclipses, respectively. The periodicity in the O – C curves, of $P_2 \sim 52$ d, is also observed in the radial velocities (Section 4), and is thus attributed to the tertiary star of the triple system, as discussed further in Section 5.

4 SPECTROSCOPIC OBSERVATIONS AND RADIAL VELOCITY EXTRACTION

We obtained 24 spectra between 2020 January 31 and October 5 using the HERMES spectrograph ($R \sim 85\,000$, Raskin et al. 2011) on the 1.2-m Mercator telescope at Observatorio del Roque de los Muchachos at Santa Cruz de la Palma, Canary Islands, Spain. The spectra were reduced (extracted, order-merged, wavelength-calibrated) using the local HERMES pipeline (Raskin et al. 2011), and subsequently normalized using a spline fit (Abdul-Masih et al. 2021). The spectra show strong He II 4686 lines and no sign of He II 4542 lines, indicating that the dominant signal originates from an early B star. The relative strengths of the He I, He II, and Mg lines indicates that the dominant spectral contribution is consistent with that from an O9.5-B0.5V star (Sota et al. 2011). The RV shifted and median combined spectrum is shown in Fig. 4, where the bottom panels show the relative depths of pairs of diagnostic spectral lines from Sota et al. (2011) used to determine the spectral classification of the star. This spectral classification agrees with the previous estimates of the spectral class by Brodskaya (1953) and Laur et al. (2017). A spectral class of O9.5-B0.5V nominally corresponds to a 14–17-$M_\odot$ star (Harmanec 1988; Martins, Schaerer & Hillier 2005; Silaj et al. 2014).

We searched for additional signals in the spectra using Least Squares Deconvolution (LSD, Donati et al. 1997; Tkachenko et al. 2013). In brief, this technique assumes that all lines in a spectrum have a common underlying profile with varying depths depending on the particular line. This common profile is recovered by deconvolving the lines within a particular wavelength region with a line-list template with associated line depths. This method was generalised by Tkachenko et al. (2013) to allow for multiple components in a spectra and to allow for each component to draw from a different line list. Here, we calculated LSD profiles of the HERMES spectra over 4300–5200 Å, using helium, carbon, nitrogen, and silicon lines whose rest wavelengths were computed from the Vienna Atomic Line Database (VALD-II, Kupka et al. 1999). We restricted ourselves to this range to minimize the potential noise contribution from weak lines. The resulting profiles did not reveal the presence of any additional components. The radial velocities of each spectrum were computed as the centre of gravity of the LSD profiles and are listed in Table A1. Inspection of the RVs reveal the same periodic signal, of $P_2 = 52$ d, as seen in the ETVs (Section 3.3). As the $P_2 = 52$ d signal is seen in both the ETVs and the RVs, we confirm that the system is comprised of a $P_1 = 1.1047$ d eclipsing binary (stars A and B) and a $P_2 = 52$ d outer O9.5-B0.5V tertiary (star C) orbiting around a common centre of mass.

5 JOINT ETV AND RV MODELLING

In this section, we describe the joint modelling of the ETV and the RV signals assuming that they are physically associated as a triple system. There are two main effects responsible for deviations from strict periodicity in eclipse timings: the light travel time effect (LTTE; geometrical contribution) and the dynamical effect. The former is a result of a change in projected distance from the centre of mass of the binary to that of the triple. The dynamical effect, on the other hand, results from physical changes in the orbit of the binary system due to the gravitational influence of the third body (Borkovits et al. 2003).

Modelling of the ETVs allowed us to derive properties including the mass ratio of the tertiary to the total mass of the system (m_C/m_{ABC}), the eccentricity of the tertiary (e_2), and the mutual inclination between the orbital plane of the binary and the orbital plane of the tertiary(i_m). Following Borkovits et al. (2016), perturbations produced by a close third body introduce deviations to a linear

Table 2. System parameters either sampled or derived from the HMC optimization, as well as parameters estimated from the *TESS* light curve.

Parameter	Symbol	Prior	Value	Units	Model
Sampled parameters					
Orbital period tertiary	P_2	$\mathcal{N}[52.1, 2]$	$52.044^{+0.017}_{-0.017}$	d	ETV + RV
Semi-major axis, binary to COM	$a_{\rm AB}\sin i_2$	$\mathcal{U}[10, 500]$	$91.22^{+2.671}_{-10.65}$	$R_\odot$	ETV
Tertiary to total mass ratio ($m_{\rm C}/m_{\rm ABC}$)	$q_{\rm tot}$	$\mathcal{N}[0.58, 0.14]$	$0.563^{+0.032}_{-0.014}$		ETV
Tertiary eccentricity	e_2	$\mathcal{U}[0, 0.4]$	$0.30^{+0.013}_{-0.009}$		ETV + RV
Binary eccentricity	e_1	–	0		fixed
Observed argument of periastron	ω_2	$\mathcal{U}[0, 360]$	$295.7^{+6.6}_{-3.6}$	deg	ETV + RV
Mutual inclination	i_m	$\mathcal{U}[0, 360]$	$16.8^{+4.2}_{-1.4}$	deg	ETV
Dynamical argument of periastron	g_2	$\mathcal{U}[0, 360]$	$359.05^{+12.0}_{-41.2}$	deg	ETV
Semi-amplitude	$logK$	$\mathcal{N}[81, 20]$	$72.168^{+1.023}_{-1.019}$		RV
t_0 of tertiary	$t_{0,2}$	$\mathcal{N}[1878, 25]$	$1880.394^{+0.713}_{-0.267}$	BJD – 2457000	ETV + RV
Correction to T_0	c_0	$\mathcal{N}[0, 5]$	$-0.0^{+0.0000}_{-0.0001}$		ETV
Correction to P_1	c_1	$\mathcal{N}[0, 0.5]$	$-0.003^{+0.017}_{-0.009}$		ETV
Secular change to P_1	c_2	$\mathcal{N}[0, 0.0001]$	$0.237^{+0.521}_{-0.275}$		ETV
Derived parameters					
Semi-major axis, tertiary to COM	$a_{\rm C}\sin i_2$	–	$70.923^{+0.98}_{-2.03}$	$R_\odot$	RV
Project mass of binary	$m_{\rm AB}\sin^3 i_2$	–	$9.21^{+0.6}_{-1.4}$	$\mathrm{M}_\odot$	ETV + RV
Project mass of tertiary	$m_{\rm C}\sin^3 i_2$	–	$11.87^{+0.9}_{-2.9}$	$\mathrm{M}_\odot$	ETV + RV
Light curve extracted parameters					
Orbital period binary	P_1	–	$1.104\,686 \pm 0.000\,004$	d	–
t_0 of primary eclipse	$t_{0,1}$	–	1785.533	BJD – 2457000	–
SED parameters					
Mass of binary star A	$M_{\rm A}$	–	6–7	$\mathrm{M}_\odot$	SED
Mass of binary star B	$M_{\rm B}$	–	5.5–6.3	$\mathrm{M}_\odot$	SED
Mass of tertiary star C	$M_{\rm C}$	–	14.5–16	$\mathrm{M}_\odot$	SED
Luminosity of binary star A	$L_{\rm A}$	–	3.00–3.27	$\log \mathrm{L}/L_\odot$	SED
Luminosity of binary star B	$L_{\rm B}$	–	3.02–3.14	$\log \mathrm{L}/L_\odot$	SED
Luminosity of tertiary star C	$L_{\rm C}$	–	4.71–4.86	$\log \mathrm{L}/L_\odot$	SED
Distance	d	–	4.0–4.5	kpc	SED
Reddening	$E(B–V)$	–	0.40–0.44		SED

ephemeris according to

$$\Delta = \sum_{i=0}^{3} c_i E^i + \left[\Delta_{\rm LTTE} + \Delta_{\rm dyn}\right]_0^E . \quad (1)$$

The first three terms multiplied by the cycle number E represent corrections to the reference epoch (c_0), the orbital period (c_1), and any secular changes to the period (c_2).

The extent of the contribution of the LTTE to the perturbation depends on the light-crossing time of the relative orbit, $a_{AB}\sin i_2/\tilde{c}$ (where $\tilde{c}$ is the speed of light), as well as the configuration of the outer orbit:

$$\Delta_{\rm LTTE} = -\frac{a_{AB}\sin i_2}{\tilde{c}} \frac{\left(1-e_2^2\right)\sin(\nu_2+\omega_2)}{1+e_2\cos\nu_2}, \quad (2)$$

where ν_2 is the true anomaly of the outer orbit, and is determined by $t_{0,2}$, P_2, and e_2. All quantities relating to the inner orbit ($P_1 \sim$1.1 d) have a subscript 1, while all quantities relating to the outer orbit ($P_2 \sim$52 d) have a subscript 2. Quantities with the subscript *AB* refer to the individual components of orbit 1, whereas quantities with the subscript *C* refer to the tertiary component in orbit 2. All symbols referring to a single quantity are explained in Table 2.

The dynamical perturbation has a more complex dependence on the mass ratio of the system, the ratio of the periods, as well as the mutual inclination of the two orbits, denoted as i_m. This term is given by

$$\Delta_{\rm dyn} = \frac{3}{4\pi}\frac{m_{\rm C}}{m_{\rm ABC}}\frac{P_1^2}{P_2}\left(1-\mathrm{e}_2^2\right)^{-3/2} \times \left[\left(\frac{2}{3}-\sin^2 i_m\right)\mathcal{M} + \frac{1}{2}\sin^2 i_m \mathcal{S}\right] \quad (3)$$

with

$$\mathcal{M} = 3e_2\sin\nu_2 - \frac{3}{4}{e_2}^2\sin 2\nu_2 + \frac{1}{3}{e_2}^3\sin 3\nu_2 \quad (4)$$

and

$$\mathcal{S} = \sin(2\nu_2+2g_2) + e_2\left[\sin(\nu_2+2g_2) + \frac{1}{3}\sin(3\nu_2+2g_2)\right]. \quad (5)$$

All symbols are explained in Table 2.

The RV variations of the tertiary component are given by

$$V = \gamma + \frac{2\pi a_C \sin i_2}{P_2\sqrt{\left(1-e_2^2\right)}}[e_2\cos(\omega_2) + \cos(\nu_2+\omega_2)]. \quad (6)$$

Here, all terms have the same subscripts as in the ETV equations, and the systemic velocity is given by γ. Given the overlap in parameters between the ETV and RV models, as well as the complementary information held in the independent data sets, we are able to constrain the systems to a high degree.

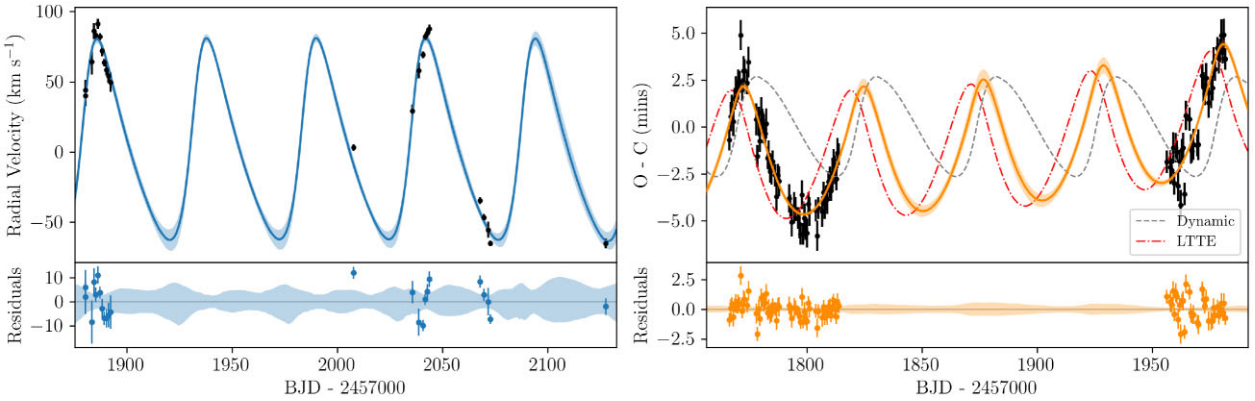

Figure 5. Joint MCMC model of the HERMES RV data (left-hand panel) and the extracted ETVs (right-hand panel). The model parameters are presented in Table 2. The bottom panels show the residuals of the best fit. The overall ETV fit is a linear addition of the dynamical effect (small dashed grey line) and the light travel time effect (large dashed red line).

Model optimization was carried out using a No U-Turn Sampling (NUTS; Hoffman & Gelman 2014) Hamiltonian Monte Carlo (HMC) approach. In short, HMC is a class of Markov chain Monte Carlo (MCMC) methods used to numerically approximate a posterior probability distribution. Whereas traditional MCMC techniques use a stochastic walk to explore a given n-dimensional parameter space, the NUTS algorithm makes use of a Hamiltonian description of probability distribution in order to more directly sample the posterior probability distribution of a set of model parameters θ given by Bayes' theorem: $p(\theta|d) \propto p(d|\theta, \sigma) \times p(\theta)$. The likelihood term $p(d|\theta, \sigma)$ is the evaluation of how well the model represents the data d given the parameters θ and uncertainties σ. In our application, the model is given by the ETVs and RV variations in equations (1) and (6), such that:

$$p\,(d|\theta, \sigma) \propto (\mathcal{M}_{ETV} - Y_{ETV}) + (\mathcal{M}_{RV} - Y_{RV})\,, \tag{7}$$

where $\mathcal{M}$ refers to the model and Y refers to the data.

In order to best exploit the complementary and overlapping information in the RV and ETV data, the two data sets were modelled jointly. This allowed us to simultaneously fit for, and better constrain, parameters that appear in both models (see Table 2). The joint analysis made use of the open source software packages EXOPLANET and PYMC3 (Salvatier, Wiecki & Fonnesbeck 2016; Foreman-Mackey et al. 2021). The optimal parameter values and their uncertainties were calculated as the median and 67.8 per cent highest posterior density of the marginalized posterior distributions. The priors and extracted values for all sampled parameters are given in Table 2. The best-fitting model, as constructed from the values in Table 2, for the RVs and ETVs are shown in the left- and right-hand panels of Fig. 5. We note that the residuals in the ETVs and RVs show no evidence for additional periodicities.

6 SYSTEM CONFIGURATION, STABILITY, AND EVOLUTION

6.1 Configuration

The combination of RV and photometric data revealed a dynamically interacting triple system, comprised of a close 1.1047 d eclipsing binary (stars A and B) with a massive companion on a wide, non-eclipsing, ∼52 d orbit (star C). From the dynamical modelling (presented in Section 5), we derived a mass ratio of the inner binary to the tertiary of $q = m_{\rm AB}/m_{\rm C} = a_{\rm C} \sin i_2 / a_{\rm AB} \sin i_2 = 0.7776$. Given the

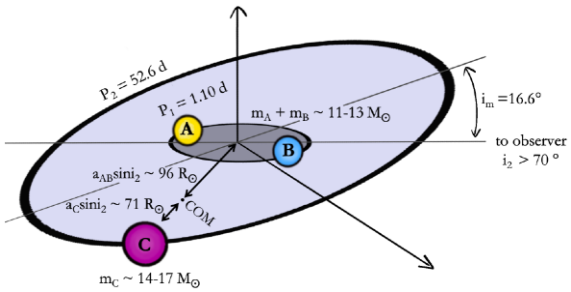

Figure 6. Schematic of the triple system. Relative sizes of the orbits are not to scale and for simplicity the orbits are depicted as circular.

spectral classification of star C, of O9.5V-B0.5V, the tertiary star has a mass in the range of 14–17 $M_\odot$, meaning that the combined mass of stars A and B is in the range of 10.9–13.2 $M_\odot$. By considering both the spectroscopic mass range of the tertiary and the estimated mutual inclination $i_{\rm m}$, we can derive limits on the inclination of both the orbit of inner binary i_1 and the orbit of the tertiary i_2 on the sky. From these considerations, we find that i_1 lies in the range: $77\overset{\circ}{.}9 \leq i_1 \leq 90^\circ$ and i_2 lies in the range: $62\overset{\circ}{.}5 \leq i_2 \leq 71\overset{\circ}{.}1$. The high inclination of i_1 agrees with the observed flat bottom, i.e. full, eclipses observed for the short 1.1 d orbit. Conversely, from the presence of flat-bottomed eclipses in the TESS light curve, we can infer that the inner binary has a large inclination: $i_1 > = 80^\circ$. By combining this inferred range with the mutual inclination derived from the ETV modelling, we arrive at an estimate for the inclination of the tertiary on the sky: $i_2 \in 59^\circ - 74^\circ$. Using this, we can infer physical ranges for $m_{\rm AB} \in 8.8 - 15.6\,M_\odot$ and $m_{\rm c} \in 10.1 - 20.3\,M_\odot$. This wide range is in agreement with the mass ranges inferred from the spectral type of the tertiary star. An overview of the triple system is presented in Fig. 6. We note that while the triple and the 0.5 arcsec companion star, TIC 470710327′, are statistically associated, the companion is not assumed to have a detectable effect on the observed dynamics of the triple given its separation and short period covered by the observations.

In addition to the eclipsing $P_1 = 1.1047$ d binary signal, the *TESS* light curve contains two further periodic eclipsing signals with $P_3 = 9.9733$ d and $P_4 = 4.092$ d. The bottom panel of Fig. 2 displays the *TESS* light curve phase folded on P_3 (middle panel) and P_4 (right-hand panel). We note that due to the lack of visible 'secondary' eclipses, we cannot distinguish between periods of P_3 and P_4 or twice those values. We can, however, determine that all three sets of eclipses

are of different objects, as the morphology of all of the eclipses are constant in time, and points of overlap between the 1.10 and 9.97 d signal are reproduced as linear additions of the different eclipse signals. Furthermore, we see no dynamical evidence in the RVs or the ETVs of either the 9.97 or the 4.09 d signals being part of the same system. Using Equation 3, we can show that a dynamically interacting body with $P_3 = 9.97$ d would produce an amplitude in the ETVs that is at least $(9.97/1.10)^2 = 82$ times larger than the dynamical amplitude induced by the $P_2 = 52$ d tertiary. We see no evidence of this signal in the data. Using the same argument we also find no evidence of the $P_4 = 4.09$ d signal being associated with the tertiary star of the triple. We note that $P_1 = 1.10$ d and $P_3 = 9.97$ d is close to a 1:9 resonance ($P_3/P_1 = 9.028$). While this could indicate that the signals are related, we do not have sufficient data at present to further investigate their association.

As noted above, the presence of two additional bright sources in the *TESS* aperture, at separations of 0.5 and 22 arcsec, overall contributing over ∼10 per cent of the light in the aperture, make it difficult to determine the exact source of all of the periodic signals seen in the *TESS* light curve. Through the RVs and ETVs, however, we can associate the triple system with the brightest O9.5V-B0.5V star in the data. This is further corroborated by the data obtained with the Takahashi Epsilon telescope, which has a pixel scale of 1.64 arcsec, which allowed us to confirm that the $P_1 = 1.10$ d signal lies on the O9.5V-B0.5V target star and not the 22 arcsec companion star that lies within the same *TESS* aperture.

6.2 SED Modelling

We investigate the properties of the components of this system via grid-fitting analysis of the composite spectral energy distribution (SED) of TIC 470710327 and TIC 470710327′, using photometric data from Vizier (Table A4). In order to reduce the degeneracies present in composit SED modelling, we use the synthetic SEDs from a grid of MIST isochrone models (Choi et al. 2016). This enforces that all components of TIC 4707410327 and TIC 470710327′ are the same age and located at the same distance, and ensures realistic physical parameters for all components. The models are reddened according to $F_{\rm red} = 10^{-A_\lambda/2.5} F_{\rm mod}$ and $A_\lambda = E(B-V)R_\lambda$, where $E(B-V)$ is a free parameter, and R_λ is calculated according to Cardelli, Clayton & Mathis (1989). Each model is evaluated against the data using a χ^2 metric.

We fit a composite four-component SED to the observations, assuming one component for each member of the triple system, and one for the nearby 0.5 arcsec companion, TIC 470710327′. The light contributions derived in Section 3 are used to inform the model, such that the total light contribution of the triple system is fixed to 77 per cent in the V band, with the remaining 23 per cent originating from TIC 470710327′. Additionally, we enforce that the luminosity of the primary component of the close binary must be higher than that of the secondary, i.e. $L_A > L_B$. Furthermore, we adopt the spectroscopically derived mass range for the tertiary: $M_C \in 14-17\,M_\odot$ and only accept solutions that satisfy the triple system mass-ratio of $q_c = 0.776$. This results in 1019 possible solutions, which we rank according to their χ^2.

The solutions favour masses of the OB star of $M_C \in 14.5-16\,M_\odot$, whereas the solutions for the components of the close binary orbit favour a mass ratio $q_1 \in 0.9-1.0$ with masses for the primary components ranging from $M_A \in 6-7\,M_\odot$ and $M_B \in 5.5-6.3\,M_\odot$ We find solutions for TIC 470710327′ in the range of $11.5-14\,M_\odot$. We note that the values of the mass of TIC 470710327′ are correlated with the mass of TIC 470710327 C due to the imposed light

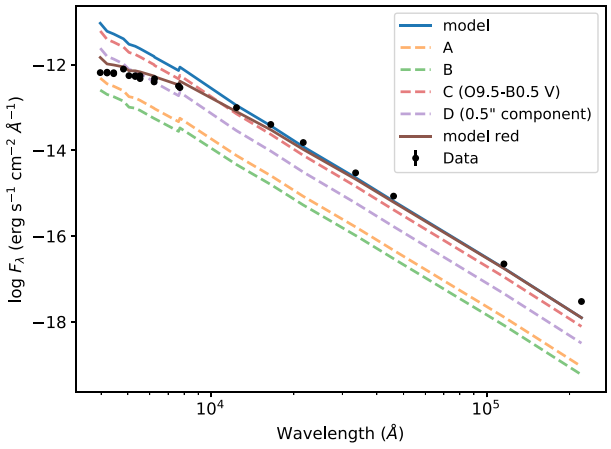

Figure 7. Observed SED (black points) with composite and individual model contributions for the best-fitting composite model. The individual contributions are unreddened, whereas we plot both the reddened (maroon) and unreddened (blue) composite models.

contributions of these objects. The model and observed SED are shown in Fig. 7. We note that this modelling returns a distance in the range of 4–4.5 kpc, whereas the *Gaia* parallax returns a distance closer to 1 kpc. In order to arrive at a distance close to the *Gaia* estimate, the reddening would need to be around 2, as opposed to the value in the range of 0.40–0.44 that we find. Although these two distances do not agree, the complexity of this system could contribute to an erroneous astrometric solution, which will likely be improved upon in future Gaia data releases.

6.3 Dynamical stability

Even though both the inner and outer orbits of the triple system are relatively compact, the separation between the two orbits ($P_2/P_1 \approx 50$) implies that the current configuration is dynamically stable. The stability criterion of Mardling & Aarseth (1999) implies long-term dynamical stability for TIC 470710327 for $P_2 \gtrsim 18$ d.

Dynamically stable systems can remain intact for many dynamical time-scales, giving rise to the possibility of observing three-body dynamics. ZKL cycles (Kozai 1962; Lidov 1962), for example, would manifest themselves as cyclic changes in the eccentricity of the inner orbit and in the mutual inclination between the inner and outer orbit. However, classical ZKL resonance can only occur in triples with mutual inclinations between 39.°2 and 140.°8, meaning that with the mutually inclined of TIC 470710327, of $\approx 16.^\circ8^{+4.^\circ18}_{-1.^\circ38}$, this effect is unlikely to be significant for the future evolution of the system.

Conversely, the higher-order effects of three-body dynamics could affect the dynamical evolution of this system (Toonen, Hamers & Portegies Zwart 2016). The eccentric ZKL mechanism (eZKL; see Naoz 2016, for a review) can give rise to more extreme eccentricity cycles for an extended range of inclinations. The magnitude of this effect can be quantified with the use of the octupole parameter (Katz, Dong & Malhotra 2011; Lithwick & Naoz 2011; Teyssandier et al. 2013; Li et al. 2014):

$$\epsilon_{\rm oct} \equiv \frac{m_{\rm A}-m_{\rm B}}{m_{\rm A}+m_{\rm B}}\frac{a_1}{a_2}\frac{e_2}{1-e_2^2} \equiv \frac{1-q_1}{1+q_1}\sqrt[3]{\frac{P_1^2}{P_2^2}(1-q_{\rm tot})}\frac{e_2}{1-e_2^2}. \quad (8)$$

The eZKL mechanism is expected to be important for the evolution of the system for values of $\epsilon_{\rm oct} \gtrsim 0.001-0.01$, and under the condition that the mass ratio of the inner binary is less than unity. Given the

values in Table 2, we find $\epsilon_{\rm oct} = 0.001$ for $q \approx 0.9$ and $\epsilon_{\rm oct} = 0.01$ for $q \approx 0.3$. Given the morphology of the eclipses in the *TESS* data (and considering the substantial diluting third light), initial modelling suggests that the mass ratio of this inner binary is close to unity. Thus, the octupole term is within the range of relevance for the dynamical evolution of this system. The expected time-scale of the eZLK cycles are thought to be of order $\tau \approx 180$ yr/$\sqrt{\epsilon_{\rm oct}}$ (Antognini 2015), i.e. $\tau \approx$1800–5700 yr. We further investigated these time-scales with simulations using the TrES triple star evolution code (Toonen et al. 2016), and found the time-scales to be consistent with our analytical estimates. However, when including tides and gravitational wave radiation, the maximum amplitude of the eccentricity of the inner binary remains on the order of $e_1 \sim 0.001$. Detailed constraints on the time-scale and amplitudes of these cycles would require detailed modelling of the inner binary, which remains impossible without full radial-velocity characterization of the inner components.

6.4 Possible formation scenarios

Several theories exist pertaining to the origin of higher order multiple systems. The formation of multiple systems is dependent on fragmentation of the natal material during the formation process. Hierarchical collapse within molecular clouds eventually leads to the formation of dense stellar cores and clumps, whose collapse results in the formation of stars and clusters. Throughout this, equatorial discs are formed through the conservation of angular momentum, which in turn can become involved in the accretion process and the formation of secondary cores. However, there is still debate as to what scale of fragmentation is the main cause of observed massive multiple systems – the fragmentation of the prestellar core or fragmentation of circumstellar discs. In both cases, opacity has a large effect on the initial separations of the systems, which cannot be less than around 10 au due to the opacity limit of fragmentation (Bate 1998; Boss 1998). Therefore, it is assumed that systems at closer separations than 10 au must have migrated to their observed positions (Bate, Bonnell & Bromm 2002). Some studies present evidence of disc fragmentation creating higher order massive multiple systems during their embedded phases (e.g. Megeath, Wilson & Corbin 2005). Other effects such as dynamical interactions between other companions and discs (Eggleton & Kisseleva-Eggleton 2006) could also cause inner binaries in multiple systems to harden into close orbits. Recent modelling by Oliva & Kuiper (2020), for example, has shown how disc fragments in the discs of massive protostars form through hierarchical fragmentation along spiral arms and migrate to spectroscopic orbits.

TIC 470710327 presents an interesting puzzle in terms of its formation given our derived geometry of a close binary with a total mass lower than the tertiary star. More massive stars have shorter Kelvin–Helmholtz time-scales than those of lower masses, so one would expect that the more massive tertiary was the first star to form. However, if this was the case, it is likely that when this star reached the main sequence (before the inner binary) it would have disrupted the remaining natal material and therefore discontinued the central binary's formation. If the central binary did form first, a more consistent interpretation could be that the inner binary formed through disc fragmentation and the dynamical effects of this binary on the disc could have created a large overdensity at large radii. Such overdensities have been shown to occur in circumbinary discs in works such as Price et al. (2018). This overdensity could have accreted significant mass, perhaps accelerated by the continuing dynamical effects of the inner binary. In order for this scenario to hold the mass of the disc must have been very large, as the disc fragmentation process would not convert all the disc material into the eventual stars, and the combined mass of the stars in the tertiary system is at least 29 solar masses. However, the largest protostellar discs detected around massive young stellar objects are of order $\sim 10\,{\rm M}_\odot$ (e.g. Johnston et al. 2020, Frost et al. 2021).

An alternative explanation for the formation of TIC 470710327 is that this system is a result of the fragmentation of the prestellar core as opposed to fragmentation of a disc (e.g. Krumholz & Bonnell 2009). This is supported by the fact that additional sources surround this triple system in the local region, in the form of 0.5- and ∼22-arcsec distant companions. With a spurious association probability of $\sim 1 \times 10^{-5}$ between TIC 470710327 and the 5 arcsec companion, this closer source is expected to have formed from the same core collapse. While the more distant source at ∼22 arcsec may not be currently bound to the tertiary system, it could still have come from the same prestellar core. The core collapse scenario circumvents the mass problem described above for disc fragmentation. Should this have occurred, we can assume that the close-binary formed from one collapse event, the tertiary star from another and the distant source from yet another. The close-binary system could have been formed by disc fragmentation as described above, and its hardening into a close-orbit could have been facilitated by dynamical interactions between the 14–17 $\rm M_\odot$ star and the distant sources from others. Dynamical effects within the collapsing core could also have led to the capture of the 14–17 $\rm M_\odot$ star by the close-binary system, forming the tertiary we see today. Dedicated radiative hydrodynamical modelling could help disentangle whether core fragmentation, disc fragmentation or a combination of both resulted in the formation of TIC 470710327, whilst repeat observations of all the sources in the region could help distinguish orbits and determine which stars are bound. Furthermore, as there are currently no resolved *Gaia* parallaxes for TIC 470710327 and TIC 470710327′, we cannot concretely rule out the possibility that these two targets are just unassociated nearby objects on the sky.

6.5 Future evolution

The observed mass ratio, whereby the tertiary is more massive than the combined mass of the inner binary, implies that the remainder of this system's evolution will be driven by the evolution of the tertiary as this star will be the first to evolve off the main sequence. Given the expected mass of the tertiary of 14–17 $\rm M_\odot$, star C is expected to fill its Roche lobe at an age of ∼ 13 Myr, at which point it will start transferring mass towards the inner binary. This type of mass transfer, from an outer star to an inner binary, is expected to occur in ∼1 per cent of all triple systems in the Massive Star Catalogue (de Vries, Portegies Zwart & Figueira 2014; Hamers, Glanz & Neunteufel 2021a).

The outcome of such a mass transfer phase is, inherently, a hydrodynamical problem (de Vries et al. 2014; Portegies Zwart & Leigh 2019). If the inner binary is compact enough such that the mass transfer stream intersects itself, a circumbinary disc may form. Leigh et al. (2020b) argue that such a scenario leads to preferential accretion to the lowest mass star of the inner binary and therefore favours evolution towards equal mass inner binary stars. The circularization radius of the mass transfer material (Frank, King & Raine 2002; Toonen et al. 2016) is around $20R_\odot$. As the inner binary has an orbital separation of $\sim 10R_\odot$, a disc may form, but it is not clear from simple analytical calculation whether that disc would be stable enough to allow for secular accretion. If the mass transfer stream intersects the trajectory of the inner two stars in their orbit around each other, friction may reduce the orbit (de Vries et al. 2014) to lead to a contact system and/or a merger. Such a merger remnant may be

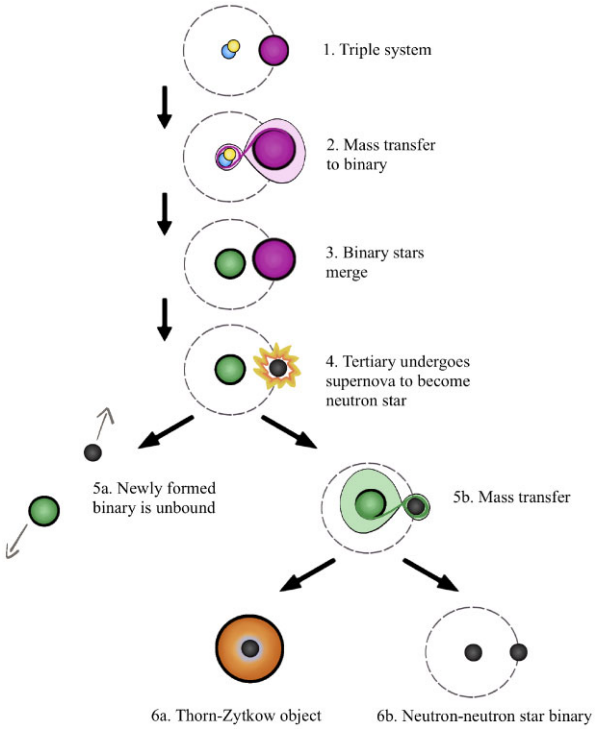

Figure 8. Possible future evolution of TIC 470710327. Relative sizes of the stars and orbits are not to scale. For simplicity, all orbits are depicted as circular.

considered a blue straggler for two reasons: it would be rejuvenated due to the merger and due to the accretion from the tertiary star.

Assuming a merger does take place, the triple would reduce to a binary system (stage 3 in Fig. 8). After the mass transfer phase ends the merger remnant would have a mass of 12–18 $M_\odot$ depending on how efficiently the binary was able to accrete matter. Given the mass of the former donor star it will evolve to become a neutron star. With typical post-mass transfer periods of several hundreds of days (i.e. orbital velocities of around 100 km s^{-1}), typical natal kicks from the supernova explosion, with magnitudes of several hundreds of km s^{-1}, would unbind the newly formed binary into two single stars (Hobbs et al. 2005; Verbunt, Igoshev & Cator 2017; Igoshev 2020), reducing the multiplicity of the system once more (5a in Fig. 8). If the orientation of the supernova kick is such that the binary remains intact the binary would likely undergo an additional mass transfer phase when the merger remnant evolves off the main-sequence. Given the large mass ratio of such a binary, the mass transfer would lead to a common-envelope phase (Ivanova et al. 2013). Consequently, this could either lead to a merger and the formation of a Thorne–Żytkow object (whereby the neutron star is enclosed by the red giant star, 6a in Fig. 8; Thorne & Zytkow 1975; Podsiadlowski, Cannon & Rees 1995; Levesque et al. 2014; Tabernero et al. 2021) or, if the binary survives, experience an ultra-stripped supernova (Tauris et al. 2015) and end up as a double neutron star (6b in Fig. 8).

7 CONCLUSIONS

TIC 470710327 is a compact, hierarchical triple system consisting of a 1.10 d binary containing two B-type stars and an OB-type tertiary on a wide 52 d orbit. The system was initially identified in *TESS* data by citizen scientists taking part in the PHT project. Using publicly available *TESS* data and newly obtained HERMES data, we report on the dynamical modelling of the system to reveal a rare configuration wherein the tertiary object in the wide orbit is more massive than the combined mass of the inner binary (m_{AB} = 10.9−13.2 $M_\odot$, m_C = 14−17 $M_\odot$). This configuration poses several challenges to explain its formation. Given the current mass of the tertiary component, star C is expected to fill its Roche lobe at an age of ∼13 Myr, meaning that the system must necessarily be younger than this age. Considering that the main-sequence lifetime of a 5.5–7 $M_\odot$ star is between 40–80 Myr, all of the stars in this system are currently in the main-sequence phase of their evolution. Furthermore, given the values from the dynamical modelling and constrained SED modelling, the primary binary component (star A) will fill between 70 and 83 per cent of its Roche lobe before the tertiary evolves off the main sequence, while the secondary binary component (star B) will fill between 68 and 75 per cent of its Roche lobe during this time. This means that the binary will not undergo mass transfer before experiencing Roche lobe overflow from the tertiary.

Given the compact orbits and the unusually high mass of the tertiary object, we speculate that the future evolution of this system will minimally involve one episode of mass transfer as the massive tertiary evolves across the Hertzsprung gap. Based on its initial mass, the tertiary will likely end its life as a neutron star. Alternatively, depending on the rate and efficiency of the mass transfer to the inner binary, the tertiary could evolve into an intermediate mass stripped star (Götberg et al. 2020). Should the binary system remain bound after the expected supernova kick (or supernovae kicks), this system could result in a close double neutron star gravitational wave progenitor, or an exotic Thorne–Żytkow object. Detection of more systems similar to TIC 470710327 would provide constraints on potential progenitor systems to gravitational wave events.

In addition to the triple system we report on two nearby stars that significantly contribute to the *TESS* aperture, located at angular separations of 22 arcsec (LS I + 61 72) and 0.5 arcsec (TIC 470710327′). Given the field density of stars around TIC 470710327, determined using Gaia eDR3, and the magnitude contrast between the target and the 0.5 arcsec companion, we show that the spurious association probability between TIC 470710327 and TIC 470710327′ is $\sim 1 \times 10^{-5}$. These two nearby stars may be the source of the two additional periodic signals ($P_3 = 9.97$ d and $P_4 = 4.01$ d) seen in the *TESS* light curve. Additional photometric observations of the nearby stars are needed in order to probe the origins of the P_3 and P_4 and to determine the true multiplicity of this complex system.

With further observational characterization, particularly aimed at characterizing the nature of the inner binary, this system stands to become an excellent target to scrutinize simulations of massive star formation and evolution. Future spectroscopic observations that are specifically aimed at detecting the RV variations of both components of the inner binary would allow us to place tighter constraints on the dynamics of the system. In particular, these observations would allow us to probe the eZKL mechanism. Finally, RV characterization and detailed eclipse modelling of the inner binary would precisely constrain the light contributions of all components of the triple system. With such constraints, derivations of the atmospheric properties, such as $T_{\rm eff}$, log g, $v_{\rm rot}$, and $L_{\rm bol}$ would allow us to further test whether the three stars are coeval.

ACKNOWLEDGEMENTS

We thank the referee for their helpful comments that improved the manuscript. We thank all of the citizen scientists who take part in the Planet Hunters TESS project and who enable the discovery of exciting planet and stellar systems in TESS data. NE also thanks the LSSTC Data Science Fellowship Program, which is funded by LSSTC, NSF Cybertraining Grant number 1829740, the Brinson

Foundation, and the Moore Foundation; her participation in the program has benefited this work. Furthermore, NE and SA acknowledge support from the UK Science and Technology Facilities Council (STFC) under grant codes ST/R505006/1 and consolidated grant no. ST/S000488. This work also received funding from the European Research Council (ERC) under the European Union's Horizon 2020 research and innovation program (Grant agreement No. 865624). CJ has received funding from NOVA, the European Research Council under the European Union's Horizon 2020 research and innovation programme (N°670519:MAMSIE), and from the Research Foundation Flanders under grant agreement G0A2917N (BlackGEM). ST acknowledge support from the Netherlands Research Council NWO (VENI 639.041.645 grants). PGB was supported by NAWI Graz. SJ acknowledges support from the FWO PhD fellowship under project 11E1721N. KZAC acknowledges support under grant P/308614 of the IAC, which is financed by funds transferred from the Spanish Ministry of Science, Innovation and Universities (MCIU).

Some of the data presented in this paper were obtained from the Mikulski Archive for Space Telescopes (MAST). STScI is operated by the Association of Universities for Research in Astronomy, Inc., under NASA contract NAS5-26555. Support for MAST for non-*HST* data is provided by the NASA Office of Space Science via grant NNX13AC07G and by other grants and contracts. This paper includes data collected with the *TESS* mission, obtained from the MAST data archive at the Space Telescope Science Institute (STScI). Funding for the TESS mission is provided by the NASA Explorer Program. STScI is operated by the Association of Universities for Research in Astronomy, Inc., under NASA contract NAS 5-26555.

This work has made use of data from the European Space Agency (ESA) mission *Gaia* (https://www.cosmos.esa.int/gaia), processed by the *Gaia* Data Processing and Analysis Consortium (DPAC, https://www.cosmos.esa.int/web/gaia/dpac/consortium). Funding for the DPAC has been provided by national institutions, in particular the institutions participating in the *Gaia* Multilateral Agreement.

Based on observations made with the Mercator Telescope, operated on the island of La Palma by the Flemish Community, at the Spanish Observatorio del Roque de los Muchachos of the Instituto de Astrofísica de Canarias. Based on observations obtained with the HERMES spectrograph on the Mercator telescope, which is supported by the Research Foundation – Flanders (FWO), Belgium, the Research Council of KU Leuven, Belgium, the Fonds National de la Recherche Scientifique (F.R.S.-FNRS), Belgium, the Royal Observatory of Belgium, the Observatoire de Genéve, Switzerland and the Thüringer Landessternwarte Tautenburg, Germany.

Finally, NE and CJ wish to thank the Harry Potter franchise for providing us with the in-house nickname for this system of *Fluffy*, inspired by Hagrid's three-headed dog in Harry Potter and the Philosopher's Stone.

DATA AVAILABILITY

The *TESS* data used within this paper are hosted and made publicly available by the Mikulski Archive for Space Telescopes (MAST, http://archive.stsci.edu/tess/). The *TESS* data described here may be obtained from https://dx.doi.org/10.17909/t9-5z05-k040. Similarly, the PHT classifications made by the citizen scientists can be found on the Planet Hunters Analysis Database (PHAD, https://mast.stsci.edu/phad/), which is also hosted by MAST.

Original HERMES spectra, and the newly obtained photometric data are available upon request.

This work made use of Astropy, a community-developed core PYTHON package for Astronomy (Astropy Collaboration et al. 2013, 2018), MATPLOTLIB (Hunter 2007), PANDAS (McKinney et al. 2010), NUMPY (Walt, Colbert & Varoquaux 2011), ASTROQUERY (Ginsburg et al. 2019), SKLEARN (Pedregosa et al. 2011), EXOPLANET (Foreman-Mackey et al. 2021) and PYMC3 (Salvatier, Wiecki & Fonnesbeck 2016).

REFERENCES

Abdul-Masih M. et al., 2021, A&A, 651, A96
Aldoretta E. J. et al., 2015, AJ, 149, 26
Ammons S. M., Robinson S. E., Strader J., Laughlin G., Fischer D., Wolf A., 2006, ApJ, 638, 1004
Antognini J. M. O., 2015, MNRAS, 452, 3610
Antonini F., Toonen S., Hamers A. S., 2017, ApJ, 841, 77
Astropy Collaboration et al., 2018, AJ, 156, 123
Barbary K., 2016, J. Open Source Softw., 1, 58
Bastian N., Covey K. R., Meyer M. R., 2010, ARA&A, 48, 339
Bate M. R., 1998, ApJ, 508, L95
Bate M. R., Bonnell I. A., Bromm V., 2002, MNRAS, 336, 705
Bertin E., Arnouts S., 1996, A&AS, 117, 393
Bodensteiner J. et al., 2021, A&A, 652, A70
Borkovits T. et al., 2021, MNRAS, 503, 3759
Borkovits T., Érdi B., Forgács-Dajka E., Kovács T., 2003, A&A, 398, 1091
Borkovits T., Rappaport S., Hajdu T., Sztakovics J., 2015, MNRAS, 448, 946
Borkovits T., Hajdu T., Sztakovics J., Rappaport S., Levine A., Bíró I. B., Klagyivik P., 2016, MNRAS, 455, 4136
Boss A. P., 1998, ApJ, 501, L77
Bourges L., Mella G., Lafrasse S., Duvert G., Chelli A., Le Bouquin J. B., Delfosse X., Chesneau O., 2017, VizieR Online Data Catalog, p. II/346
Brodskaya E. S., 1953, Izvestiya Ordena Trudovogo Krasnogo Znameni Krymskoj Astrofizicheskoj Observatorii, 10, 104
Cardelli J. A., Clayton G. C., Mathis J. S., 1989, ApJ, 345, 245
Choi J., Dotter A., Conroy C., Cantiello M., Paxton B., Johnson B. D., 2016, ApJ, 823, 102
Conroy K. E., Prša A., Stassun K. G., Orosz J. A., Fabrycky D. C., Welsh W. F., 2014, AJ, 147, 45
Cutri R. M., et al., 2013, VizieR Online Data Catalog, p. II/328
de Mink S. E., Langer N., Izzard R. G., Sana H., de Koter A., 2013, ApJ, 764, 166
de Mink S. E., Sana H., Langer N., Izzard R. G., Schneider F. R. N., 2014, ApJ, 782, 7
de Vries N., Portegies Zwart S., Figueira J., 2014, MNRAS, 438, 1909
Dib S., Schmeja S., Hony S., 2017, MNRAS, 464, 1738
Donati J. F., Semel M., Carter B. D., Rees D. E., Collier Cameron A., 1997, MNRAS, 291, 658
Eggleton P. P., Kisseleva-Eggleton L., 2006, Ap&SS, 304, 75
Eisner N. L. et al., 2021, MNRAS, 501, 4669
Fabricius C., Høg E., Makarov V. V., Mason B. D., Wycoff G. L., Urban S. E., 2002, A&A, 384, 180
Foreman-Mackey D. et al., 2021, JOSS, 6, 3285
Frank J., King A., Raine D. J., 2002, Accretion Power in Astrophysics: Third Edition. Accretion Power in Astrophysics. Cambridge Univ. Press, Cambridge
Frost A. J., Oudmaijer R. D., Lumsden S. L., de Wit W. J., 2021, ApJ, 920, 48
Gaia Collaboration et al., 2016, A&A, 595, A1
Gaia Collaboration et al., 2018, A&A, 616, A1
Gaia Collaboration et al., 2021, A&A, 650, C3
Ginsburg A. et al., 2019, AJ, 157, 98
Glanz H., Perets H. B., 2021, MNRAS, 500, 1921
Götberg Y., Korol V., Lamberts A., Kupfer T., Breivik K., Ludwig B., Drout M. R., 2020, ApJ, 904, 56
Hajdu T., Borkovits T., Forgács-Dajka E., Sztakovics J., Marschalkó G., Benkő J. M., Klagyivik P., Sallai M. J., 2017, MNRAS, 471, 1230
Hamers A. S., Glanz H., Neunteufel P., 2021a, preprint (arXiv:2110.00024)
Hamers A. S., Rantala A., Neunteufel P., Preece H., Vynatheya P., 2021b, MNRAS, 502, 4479

Harmanec P., 1988, Bull. Astron. Inst. Czech., 39, 329
Hartkopf W. I. et al., 2000, AJ, 119, 3084
Hartkopf W. I., Mason B. D., Rafferty T. J., 2008, AJ, 135, 1334
Henden A. A., Templeton M., Terrell D., Smith T. C., Levine S., Welch D., 2016, VizieR Online Data Catalog, p. II/336
Hobbs G., Lorimer D. R., Lyne A. G., Kramer M., 2005, MNRAS, 360, 974
Hoffman M. D., Gelman A., 2014, J. Mach. Learn. Res., 15, 1593
Howell S. B., Everett M. E., Sherry W., Horch E., Ciardi D. R., 2011, AJ, 142, 19
Hunter J. D., 2007, Comput. Sci. Eng., 9, 90
Igoshev A. P., 2020, MNRAS, 494, 3663
Ito T., Ohtsuka K., 2019, Monogra. Environ. Earth Planets, 7, 1
Ivanova N. et al., 2013, A&A Rev., 21, 59
Jenkins J. M. et al., 2016, in Proc. SPIE. p. 99133E
Johnston K. G. et al., 2020, A&A, 634, L11
Katz B., Dong S., Malhotra R., 2011, Phys. Rev. Lett., 107, 181101
Kiminki D. C., Kobulnicky H. A., 2012, ApJ, 751, 4
Kochanek C. S. et al., 2017, Publ. Astron. Soc. Pac., 129, 104502
Kozai Y., 1962, AJ, 67, 591
Krumholz M. R., Bonnell I. A., 2009, in G. Chabrier, ed., Structure Formation in Astrophysics. Cambridge Univ. Press, Cambridge, p. 288
Kupka F., Piskunov N., Ryabchikova T. A., Stempels H. C., Weiss W. W., 1999, Astron. Astrophys. Suppl. Ser., 138, 119
Lasker B. M. et al., 2008, AJ, 136, 735
Laur J., Kolka I., Eenmäe T., Tuvikene T., Leedjärv L., 2017, A&A, 598, A108
Leigh N. W. C., Toonen S., Portegies Zwart S. F., Perna R., 2020a, MNRAS, 496, 1819
Leigh N. W. C., Toonen S., Portegies Zwart S. F., Perna R., 2020b, MNRAS, 496, 1819
Levesque E. M., Massey P., Zytkow A. N., Morrell N., 2014, MNRAS, 443, L94
Li G., Naoz S., Holman M., Loeb A., 2014, ApJ, 791, 86
Lidov M. L., 1962, Planet. Space Sci., 9, 719
Lindegren L. et al., 2021, A&A, 649, A2
Lintott C. et al., 2011, MNRAS, 410, 166
Lintott C. J. et al., 2008, MNRAS, 389, 1179
Lithwick Y., Naoz S., 2011, ApJ, 742, 94
Li M. C. A. et al., 2018, MNRAS, 480, 4557
McKinney W. et al., 2010, in van der Walt S., Millman J., eds, Proceedings of the 9th Python in Science Conference. p. 56
Maíz Apellániz J. et al., 2019, A&A, 626, A20
Mardling R., Aarseth S., 1999, in Steves B. A., Roy A. E., eds, NATO Advanced Science Institutes (ASI) Series C Vol. 522. Kluwer Academic Publishers, p. 385
Marsh T. R., Armstrong D. J., Carter P. J., 2014, MNRAS, 445, 309
Martins F., Schaerer D., Hillier D. J., 2005, A&A, 436, 1049
Matson R. A., Howell S. B., Ciardi D. R., 2019, AJ, 157, 211
Megeath S. T., Wilson T. L., Corbin M. R., 2005, ApJ, 622, L141
Moe M., Di Stefano R., 2017, ApJS, 230, 15
Naoz S., 2016, ARA&A, 54, 441
Oliva G. A., Kuiper R., 2020, A&A, 644, A41
Pedregosa F. et al., 2011, J. Mach. Learn. Res., 12, 2825
Podsiadlowski P., Cannon R. C., Rees M. J., 1995, MNRAS, 274, 485
Pollacco D. L. et al., 2006, Publ. Astron. Soc. Pac., 118, 1407
Portegies Zwart S., Leigh N. W. C., 2019, ApJ, 876, L33
Price D. J. et al., 2018, MNRAS, 477, 1270
Rainot A. et al., 2020, A&A, 640, A15
Rappaport S. et al., 2017, MNRAS, 467, 2160
Raskin G. et al., 2011, A&A, 526, A69
Reed B. C., 2003, AJ, 125, 2531
Renzo M. et al., 2019, A&A, 624, A66
Ricker G. R. et al., 2015, J. Astronomical Telescopes Instrum. Sys., 1, 014003
Salpeter E. E., 1955, ApJ, 121, 161
Salvatier J., Wiecki T. V., Fonnesbeck C., 2016, PeerJ Comput. Sci., 2, e55
Sana H. et al., 2012, Science, 337, 444
Sana H. et al., 2013, A&A, 550, A107
Sana H. et al., 2014, ApJS, 215, 15
Shappee B. J. et al., 2014, ApJ, 788, 48
Silaj J., Jones C. E., Sigut T. A. A., Tycner C., 2014, ApJ, 795, 82
Sota A., Maíz Apellániz J., Walborn N. R., Alfaro E. J., Barbá R. H., Morrell N. I., Gamen R. C., Arias J. I., 2011, ApJS, 193, 24
Sriram K., Malu S., Choi C. S., Vivekananda Rao P., 2018, AJ, 155, 172
Stephan A. P. et al., 2019, ApJ, 878, 58
Tabernero H. M., Dorda R., Negueruela I., Marfil E., 2021, A&A, 646, A98
Tan J. C., Beltrán M. T., Caselli P., Fontani F., Fuente A., Krumholz M. R., McKee C. F., Stolte A., 2014, in Beuther H., Klessen R. S., Dullemond C. P., Henning T., eds, Protostars and Planets VI. University of Arizona Press, Tucson. p. 149
Tauris T. M., Langer N., Podsiadlowski P., 2015, MNRAS, 451, 2123
Teyssandier J., Naoz S., Lizarraga I., Rasio F. A., 2013, ApJ, 779, 166
Thorne K. S., Zytkow A. N., 1975, ApJ, 199, L19
Tkachenko A., Van Reeth T., Tsymbal V., Aerts C., Kochukhov O., Debosscher J., 2013, A&A, 560, A37
Toonen S., Hamers A., Portegies Zwart S., 2016, Comput. Astrophys. Cosmol., 3, 6
Verbunt F., Igoshev A., Cator E., 2017, A&A, 608, A57
von Zeipel H., 1910, Astron. Nachr., 183, 345
Walt S. v. d., Colbert S. C., Varoquaux G., 2011, Comput. Sci. Eng., 13, 22
Zacharias N., Finch C. T., Girard T. M., Henden A., Bartlett J. L., Monet D. G., Zacharias M. I., 2013, AJ, 145, 44
Ziegler C. et al., 2018, AJ, 156, 259
Zinnecker H., Yorke H. W., 2007, ARA&A, 45, 481

APPENDIX A: ADDITIONAL TABLES

Summary of the RV observations obtained with the HERMES spectrograph (Section 4), ETVs determined from the *TESS* data (Section 3.3 and inputs used for the SED analysis (Section 6.2).

Table A1. RV observations for TIC 470710327.

Time (BJD – 2457000)	RV (km s^{-1})	RV err (km s^{-1})	S/N
1880.3395	0.03	7.19	45
1880.3518	4.22	7.11	45
1883.3908	24.25	9.00	27
1884.3813	46.12	5.78	59
1885.3333	43.12	3.10	85
1886.3368	51.28	3.63	80
1887.3369	42.11	2.51	91
1888.3537	32.07	4.07	75
1889.3285	23.70	2.72	89
1890.3321	18.43	3.81	78
1891.3247	14.30	5.07	66
1892.3270	9.70	6.93	47
2007.7168	– 36.85	2.45	92
2035.6305	– 10.77	4.62	70
2038.6952	18.08	5.63	60
2040.6938	29.27	2.40	92
2041.6919	42.08	2.41	92
2042.6432	44.82	3.16	85
2043.6680	47.71	3.19	84
2067.7128	– 74.50	2.49	91
2069.7160	– 86.61	2.48	91
2071.7410	– 95.40	5.67	60
2072.7397	– 105.13	2.00	96
2127.5437	– 105.09	3.46	82

Table A2. O – C values for the primary eclipses.

Cycle number	Predicted linear ephemeris epoch (BJD – 2457000)	O – C (mins)	Error (mins)
0	1766.2700	– 0.684	0.582
1	1767.3747	1.147	0.583
2	1768.4794	1.510	0.577
3	1769.5841	1.908	0.594
4	1770.6887	2.403	0.592
5	1771.7934	1.995	0.590
6	1772.8981	3.012	0.604
7	1774.0028	2.351	0.603
11	1778.4215	– 1.554	0.599
12	1779.5262	– 0.756	0.584
13	1780.6309	0.378	0.581
14	1781.7356	– 0.343	0.609
15	1782.8403	– 1.649	0.589
16	1783.9450	– 2.364	0.602
17	1785.0497	– 1.846	0.580
18	1786.1543	– 2.562	0.594
19	1787.2590	– 2.571	0.598
24	1792.7825	– 4.193	0.599
25	1793.8871	– 10.852	0.597
26	1794.9918	– 4.375	0.644
27	1796.0965	– 4.856	0.577
28	1797.2012	– 5.707	0.563
29	1798.3059	– 5.709	0.575
30	1799.4106	– 5.429	0.591
31	1800.5153	– 4.098	0.605
34	1803.8293	– 4.444	0.581
35	1804.9340	– 4.312	0.584
36	1806.0387	0.786	0.554
37	1807.1434	– 3.490	0.568
38	1808.2480	– 3.775	0.649
39	1809.3527	– 2.923	0.562
40	1810.4574	– 3.381	0.563
41	1811.5621	– 1.754	0.566
42	1812.6668	– 2.763	0.608
43	1813.7715	– 1.453	0.587
172	1956.2759	– 1.853	0.587
174	1958.4853	– 2.323	0.625
175	1959.5900	– 3.002	0.590
176	1960.6946	– 1.307	0.591
177	1961.7993	– 1.815	0.592
178	1962.9040	– 1.221	0.594
179	1964.0087	– 3.575	0.594
181	1966.2181	0.422	0.629
182	1967.3228	– 1.289	0.599
184	1969.5321	– 0.969	0.583
186	1971.7415	2.736	0.627
187	1972.8462	1.779	0.615
188	1973.9509	– 3.132	0.593
190	1976.1602	2.088	0.657
191	1977.2649	3.076	0.611
192	1978.3696	4.212	0.594
193	1979.4743	4.072	0.623
194	1980.5790	3.980	0.597
195	1981.6837	3.632	0.582

Table A3. O – C values for the secondary eclipses.

Cycle number	Predicted linear ephemeris epoch (BJD – 2457000)	O – C (mins)	Error (mins)
0.5	1766.8223	0.552	0.773
1.5	1767.9270	0.284	0.775
2.5	1769.0317	1.908	0.789
3.5	1770.1364	2.266	0.805
4.5	1771.2411	4.902	0.796
5.5	1772.3458	2.988	0.786
6.5	1773.4505	– 4.964	0.792
7.5	1774.5551	3.468	0.821
10.5	1777.8692	0.403	0.850
11.5	1778.9739	0.303	0.784
12.5	1780.0786	0.757	0.829
13.5	1781.1833	– 0.089	0.791
14.5	1782.2879	0.185	0.807
15.5	1783.3926	– 1.492	0.779
16.5	1784.4973	– 2.271	0.794
18.5	1786.7067	– 3.702	0.791
19.5	1787.8114	– 2.883	0.804
23.5	1792.2301	– 3.806	0.763
24.5	1793.3348	– 5.062	0.774
25.5	1794.4395	– 4.309	0.836
27.5	1796.6489	– 5.181	0.763
28.5	1797.7535	– 3.611	0.768
29.5	1798.8582	– 4.852	0.784
30.5	1799.9629	– 5.658	0.776
31.5	1801.0676	– 4.506	0.775
34.5	1804.3816	– 5.796	0.804
36.5	1806.5910	– 4.506	0.809
37.5	1807.6957	– 4.097	0.810
38.5	1808.8004	– 3.854	0.777
39.5	1809.9051	– 2.949	0.835
40.5	1811.0098	– 2.466	0.834
41.5	1812.1144	– 2.277	0.770
42.5	1813.2191	– 1.383	0.811
173.5	1957.9329	– 2.145	0.897
174.5	1959.0376	– 1.105	0.832
175.5	1960.1423	– 1.108	0.793
176.5	1961.2470	– 3.146	0.809
177.5	1962.3517	– 4.163	0.813
178.5	1963.4564	– 1.103	0.814
179.5	1964.5610	0.615	0.783
180.5	1965.6657	1.774	0.794
181.5	1966.7704	– 1.163	0.793
182.5	1967.8751	– 0.928	0.813
184.5	1970.0845	– 0.943	0.816
186.5	1972.2938	2.103	0.830
187.5	1973.3985	2.611	0.797
188.5	1974.5032	1.298	0.807
189.5	1975.6079	1.833	0.832
190.5	1976.7126	3.443	0.803
191.5	1977.8173	7.375	0.819
192.5	1978.9220	3.657	0.796
193.5	1980.0266	4.875	0.860
194.5	1981.1313	4.909	0.859

Table A4. Photometric observations of TIC 470710327.

Pass band	Effective wavelength (Å)	Flux (erg $s^{-1}cm^{-2}Å^{-1}$)	Magnitude	Ref.
Johnson:U	3971.00	6.52e-13 ± 3.26e-14	9.38	*a*
HIP:BT	4203.01	6.40e-13 ± 1.19e-14	9.40	*b*
HIP:BT	4203.01	6.65e-13 ± 1.53e-14	9.36	*c*
Johnson:B	4442.03	6.17e-13 ± 1.37e-14	9.44	*d*
Johnson:B	4442.03	6.47e-13 ± 1.82e-14	9.39	*e*
SDSS:g'	4819.97	7.88e-13 ± 7.62e-16	9.17	*f*
GAIA2:Gbp	5046.16	5.53e-13 ± 2.35e-15	9.56	*g*
HIP:VT	5318.96	5.30e-13 ± 9.54e-15	9.60	*b*
HIP:VT	5318.96	5.51e-13 ± 1.27e-14	9.56	*c*
Johnson:V	5537.05	5.48e-13 ± 5.28e-14	9.57	*d*
Johnson:V	5537.05	4.73e-13 ± 9.78e-15	9.73	*f*
GAIA2:G	6226.21	3.96e-13 ± 1.55e-15	9.92	*g*
SDSS:r'	6246.98	4.70e-13 ± 1.54e-14	9.73	*f*
SDSS:i'	7634.91	3.17e-13 ± 7.19e-16	10.16	*f*
GAIA/GAIA2:Grp	7724.62	2.91e-13 ± 1.51e-15	10.25	g
2MASS:J	12390.1	9.94e-14 ± 1.76e-15	11.42	*h*
2MASS:H	16 494.77	4.02e-14 ± 1.10e-15	12.40	*h*
2MASS:Ks	21 637.85	1.52e-14 ± 2.56e-16	13.46	*h*
WISE:W1	33 500.11	2.99e-15 ± 5.34e-17	15.23	*h*
WISE:W2	46 000.19	8.56e-16 ± 1.56e-17	16.58	*i*
WISE:W3	115 598.23	2.24e-17 ± 6.73e-19	20.54	*i*
WISE:W4	220 906.68	2.98e-18 ± 3.93e-19	22.73	*i*

Note. Data obtained from VizieR (http://vizier.unistra.fr/vizier/sed/). Data from [a]Reed (2003); [b]Fabricius et al. (2002); [c]Bourges et al. (2017); [d] Ammons et al. (2006); [e]Lasker et al. (2008); [f] Henden et al. (2016); [g]Gaia DR2 data, see acknowledgements, Gaia Collaboration et al. (2016), Gaia Collaboration et al. (2018); [h]Zacharias et al. (2013); [i]Cutri & et al. (2013)

This paper has been typeset from a TEX/LATEX file prepared by the author.